Ionization of Rydberg atoms at metallic surfaces: Influence of stray fields

Y. Pu, D. D. Neufeld, and F. B. Dunning

Department of Physics and Astronomy and the Rice Quantum Institute, Rice University MS61, Houston, Texas 77005-1892, USA

The ionization of xenon Rydberg atoms at metallic surfaces is examined. The data show that, when the effects of stray electric "patch" fields present on the surface are taken into account, ionization is well described by a simple over-the-barrier model. The patch fields are determined from direct measurements of the potential variations across the target surfaces using Kelvin probe force microscopy. Monte Carlo techniques are used to model the atom-surface interaction. The results confirm the important role that patch fields can play during Rydberg atom-surface interactions and suggest that such interactions can provide a sensitive probe of stray fields at surfaces.

I. INTRODUCTION

Rydberg atoms in which one electron is excited to a state of large principal quantum number n form a sensitive probe of atom-surface interactions. Because of their large physical size ($\sim n^2$ a.u.) and weak binding, even relatively far from a surface the motion of the excited electron can be strongly affected by image charge interactions, leading to the formation of hybridized Stark-like states [1–3]. Ionization can occur through resonant tunneling of the excited electron into a vacant level in the surface. Earlier studies of such resonant tunneling using xenon Rydberg atoms incident on a Au(111) surface suggested that ionization occurred over a much broader range of atom-surface separations than suggested by theory [4–10]. One possible explanation proposed for this discrepancy was the presence of local stray electric "patch" fields near the surface resulting from potential variations across the surface associated with surface inhomogeneities. Model calculations undertaken assuming a simple periodic variation in potential and an over-the-barrier model showed that such patch fields might indeed account for the experimental observations [11].

In the present work, we have measured directly the potential variations across the target surfaces using Kelvin probe force microscopy [12,13]. This information is used, together with Monte Carlo simulations and the over-the-barrier model, to predict surface ionization efficiencies for atoms with different values of n and angles of incidence. (In the over-the-barrier model it is assumed that ionization occurs as soon as the height of the barrier in the electron potential between the atom and the surface dips below the energy of the electron.) Comparison of the results of these simulations with experimental data reveals remarkably good agreement, indicating that, when the effects of patch fields are taken into account, ionization of xenon Rydberg atoms at metallic surfaces is well described using an over-the-barrier model. The data demonstrate the important role that patch fields can play during atom-surface interactions and suggest that Rydberg atoms can provide a sensitive probe of stray fields at surfaces. Understanding of such stray fields is important in studies of short-range surface phenomena such as the Casimir-Polder force [14] and noncontact friction [15,16], or when trapping atoms or ions near a surface [17,18].

II. EXPERIMENTAL METHOD

The present apparatus is described in detail elsewhere [10,19]. Briefly, xenon atoms are directed at near-grazing incidence onto the target surface. Ions formed by tunneling are attracted to the surface by their image charge fields. These fields are large and rapidly accelerate ions to the surface, where they are lost through Auger neutralization. To prevent this, an ion collection field is applied perpendicular to the surface. The initial image charge field experienced by an ion, and hence the external field required to counteract it, depends on the initial atom-surface separation at which ionization occurs, suggesting that the ionization distance can be determined from measurements of the surface ionization signal as a function of applied field.

The xenon Rydberg atoms are created by photoexciting the $^3P_0$ atoms contained in a beam of $Xe(^3P_{0,2})$ metastable atoms that is produced by electron impact excitation of ground-state atoms contained in a supersonic expansion. To obtain a well-defined angle of incidence, the atom beam is tightly collimated using an ~ 80-μm-wide $\times$ 4-mm-high aperture located ~ 1.5 cm upstream from the point of impact with the target surface. $Xe(n\mathrm{f})$ Rydberg atoms are created close to the target surface and in near-zero field using the output of an extra-cavity doubled, frequency-stabilized Ti:sapphire laser. Experiments are conducted in a pulsed mode. The laser output is formed into a train of pulses of ~ 1 μs duration and ~ 3 kHz repetition frequency using an acousto-optical modulator. Immediately after excitation, a strong pulsed field with ~ 1 μs rise time and 20 μs duration is applied to establish the ion collection field. As the field increases, the initial $Xe(n\mathrm{f})$ states correlate with the lowest members of their neighboring Stark n manifolds. Arrival time gating is used to discriminate against ions not formed in atom-surface interactions. If tunneling occurs at an atom-surface separation Z_i then, for a true equipotential surface, the minimum external field required to prevent the ion striking the surface and being lost is (in a.u.)

$$F(Z_i, T_\perp) = \left(\frac{1}{2Z_i} + \sqrt{\frac{T_\perp}{Z_i}} \right)^2, \qquad (1)$$

where $T_\perp = m v_\perp^2 / 2$ and $v_\perp$ is the component of the atom velocity perpendicular to the surface at the time of ionization.

Thus, by measuring the surface ionization signal as a function of applied field, the distribution of ionization distances can, in principle, be inferred. To obtain the absolute efficiency with which Rydberg atoms striking the surface are detected as ions, the number of incident atoms must be determined. To accomplish this, the number of Rydberg atoms initially created is first measured by field ionization induced by a large pulsed electric field applied immediately after the laser pulse. This number is then corrected for radiative decay of the Rydberg atoms during their transit to the surface.

The target surfaces employed in the present studies were characterized with the aid of atomic force microscopy (AFM) and Kelvin probe force microscopy [12,13]. While measurements of surface topography using AFM are routine, reliable measurement of the surface potential using Kelvin force microscopy is more challenging and requires frequent checks of the instrument and its calibration. To determine the latter, the sample mount was electrically isolated, allowing small bias potentials to be applied to test that these were correctly reflected in the measured surface potentials [12,13].

The 100-nm-thick Au(111) samples employed here were purchased from a commercial vendor and were formed by evaporating gold onto a cleaved mica substrate. They were installed in the apparatus and studied without further treatment or cleaning. AFM measurements (in air) revealed the presence of a series of flat granular islands on the surfaces with characteristic dimensions of $\sim$300–500 nm whose individual heights typically varied by $<$10 nm. (Similar structure has been seen for gold on mica by earlier workers [20].) Variations in surface potential of up to $\sim\pm$60–70 mV were observed across these islands on length scales of $\sim$50–250 nm. In an attempt to obtain a flatter, more uniform surface, template-stripping techniques were explored [20]. The gold film was first affixed to a second substrate using a vacuum-compatible epoxy. Following this, the original mica substrate was peeled away, leaving a gold surface which AFM measurements showed to be close to atomically flat. However, potential variations across the surface were still observed and were very similar to those seen on the initial as-grown films. This similarity suggests that the potential variations on both surfaces result from the same cause, possibly changes in surface work function caused by adsorbates present on the surface [13].

The measured surface potential distribution provides a boundary condition for Laplace's equation

$$\frac{\partial^2 \phi}{\partial x^2} + \frac{\partial^2 \phi}{\partial y^2} + \frac{\partial^2 \phi}{\partial z^2} = 0, \quad (2)$$

which allows the potential to be determined at any point above the surface. Separation of the variables shows that Eq. (2) is satisfied, for $z > 0$, by linear combinations of periodic functions of the form [21]

$$\phi(x,y,z) = \sum_i \sum_j [A_{i,j} \cos(k_{xi}x + k_{yj}y) \\ + B_{i,j} \sin(k_{xi}x + k_{yj}y)] \exp[-k_z(i,j)z], \quad (3)$$

where $k_z(i,j) = \sqrt{k_{xi}^2 + k_{yj}^2}$ when the potential at the surface, taken to be $z = 0$, can be written as

$$\phi(x,y,0) = \sum_i \sum_j [A_{i,j} \cos(k_{xi}x + k_{yj}y) \\ + B_{i,j} \sin(k_{xi}x + k_{yj}y).] \quad (4)$$

This potential is simply the Fourier expansion of the surface potential and must match that measured experimentally. In practice, discrete measurements of the surface potential are made at a series of points uniformly spaced over some area $L \times L$ of the surface (typically 1×1 μm^2) and output as an $N \times N$ ($N = 512$) matrix. The spatial resolution of the individual measurements themselves is estimated to be $\sim$25 nm, based on the size of the scanning tip ($\sim$10 nm diameter) and its height above the surface ($\sim$20 nm). An example of a measured surface potential distribution is shown in Fig. 1, and its characteristics as regards the size and periods of the potential variations are typical of those seen at different positions across both as-grown and template-stripped surfaces. The surface potential is represented using a discrete Fourier series yielding the coefficients

$$A_{i,j} = \frac{2}{N^2} \sum_{m=0}^{N-1} \sum_{n=0}^{N-1} \phi\left(\frac{mL}{N}, \frac{nL}{N}, 0\right) \cos\left[\frac{2\pi(mi+nj)}{N}\right]$$

$$B_{i,j} = \frac{2}{N^2} \sum_{m=0}^{N-1} \sum_{n=0}^{N-1} \phi\left(\frac{mL}{N}, \frac{nL}{N}, 0\right) \sin\left[\frac{2\pi(mi+nj)}{N}\right], \quad (5)$$
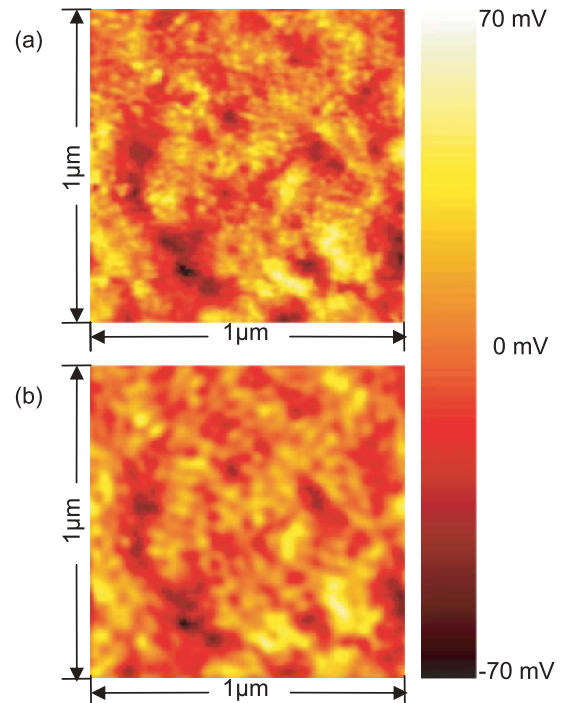
FIG. 1. (Color online) (a) Surface potential variations at a template-stripped Au(111) surface. (b) Reconstructed surface potential obtained using the 277 Fourier conjugate pairs with the largest amplitudes (see text).

where i,j are integers with values $0,1,2,\ldots,N-1$. Using these values, the potential at any point above the surface is then given by

$$\phi(x,y,z) = \sum_{i=0}^{N-1}\sum_{j=0}^{N-1}\left\{ A_{i,j}\cos\left[\frac{2\pi(ix+jy)}{L}\right] \right.$$
$$\left. + B_{i,j}\sin\left[\frac{2\pi(ix+jy)}{L}\right]\right\}\exp[-k_z(i,j)z],$$

(6)

where $k_z(i,j) = \frac{2\pi}{L}\sqrt{i^2+j^2}$. Given the strong similarities between the potential variations observed in different areas across a surface, this function, which is periodic with period L, can be used to represent the potential distribution across the entire target surface. (For an angle of incidence of $\sim 5°$, the incident Rydberg atoms illuminate an area of $\sim 1 \times 4$ mm on the target surface.) The potential $\phi(x,y,z)$ provides not only the perturbation in the potential at any point above the surface due to surface inhomogeneities but also, by taking the gradient of the potential, the local stray patch field.

In practice, not all the Fourier components present in Eq. (5) were included in the present simulations. Tests revealed that limiting the Fourier components to the 277 conjugate pairs with the largest amplitudes, which have wavelengths between 1 μm and 50 nm, produced no significant changes in the predicted surface ionization signals. It did, however, significantly reduce the computational burden while still, as illustrated in Fig. 1, yielding reconstructed surface potentials that provide a good representation of the original. (The amplitude of those Fourier components with wavelengths $\sim$50 nm is very small and the stray fields they generate decay rapidly with distance from the surface.)

To obtain an idea of the typical size of surface-induced stray fields as a function of distance from the surface, the stray fields were calculated at an array of points in a series of planes located at different distances from the surface. The root-mean-square values of these calculated fields are plotted in Fig. 2. The magnitude of the stray fields is substantial, $\sim$10–1000 V cm^{-1} at the atom-surface separations of interest here, and sufficient to significantly perturb not only Rydberg atom-surface interactions but also the ion collection fields.
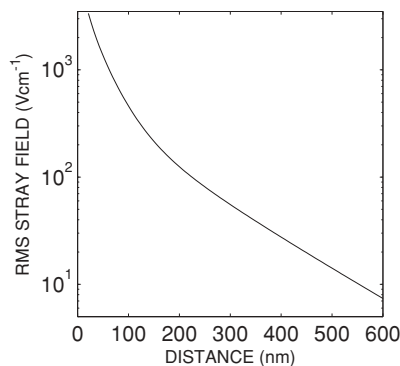
FIG. 2. Root-mean-square value of the calculated stray fields expressed as a function of distance from the surface.

III. NUMERICAL SIMULATIONS

The numerical simulations for each value of n, angle of incidence α, and applied ion collection field considered here were undertaken using a Monte Carlo approach. The incoming Rydberg atom trajectories were selected to impact random points on the surface. The initial Rydberg atom velocities were chosen at random from the known velocity distribution. Each atom is propagated toward the surface along its selected trajectory (assumed to be a straight line) and the atom-surface separation at which ionization occurs is determined using the over-the-barrier model. Following ionization, the ion trajectory is computed to see if the ion escapes the surface. The anticipated normalized surface ionization signal (i.e., the fraction of the incident Rydberg atoms that are detected as ions) is then obtained by undertaking calculations for a variety of initial Rydberg atom velocities and impact positions.

Consider a Rydberg atom with core ion coordinates X,Y,Z and electron coordinates x,y,z positioned above the surface. The electron potential (relative to that at the ion core) can be written (in a.u.) as

$$V(x,y,z) = \frac{-1}{\sqrt{\rho^2+(Z-z)^2}} - \left(\frac{1}{4z}-\frac{1}{4Z}\right)$$
$$+ \left[\frac{1}{\sqrt{\rho^2+(Z+z)^2}} - \frac{1}{2Z}\right] + F(z-Z)$$
$$- \phi(x,y,z) + \phi(X,Y,Z),$$

(7)

where $\rho^2 = (x-X)^2 + (y-Y)^2$. These terms represent, respectively, the Coulomb interaction with the ion core, the interaction of the electron with its image charge, the interaction of the electron with the image charge of the core ion, the effect of the ion collection field F, and the effect of the surface potential variations. As noted previously [10,11], a potential of the form of Eq. (7) results in the appearance of a potential barrier between the atom and surface whose height varies with the atom-surface separation, the strength of the ion collection field, and the size of the stray fields. In calculating the minimum height of this barrier, account must be taken of the fact that, because of the presence of localized variations in potential due to surface inhomogeneities, this minimum will typically not lie on the perpendicular from the surface to the core ion. A search procedure was therefore employed in which the potential along a series of straight lines radiating from the core ion toward the surface was evaluated. The step size in the polar angle, θ, measured from the $-z$ direction, was chosen to be $\Delta\theta = 3°$. The step size, $\Delta\phi$, in the azimuthal angle, ϕ, was varied with θ to keep the angular separation between adjacent lines approximately constant at $\sim 3°$. Tests revealed that the use of smaller increments for $\Delta\theta$ and $\Delta\phi$ lead to negligible changes in the final predicted results, as did limiting the search in θ to $0 \leqslant \theta \leqslant 30°$. The effect of stray fields on the barrier height is illustrated in Fig. 3. This shows the height of the barrier as a function of atom-surface separation with no stray fields present and with the effects of stray fields included for three representative incoming trajectories. The presence of stray fields dramatically influences the barrier height, which no longer decreases monotonically as the surface is approached.

To determine if ionization occurs at a particular core ion position, the height of the potential barrier is compared to
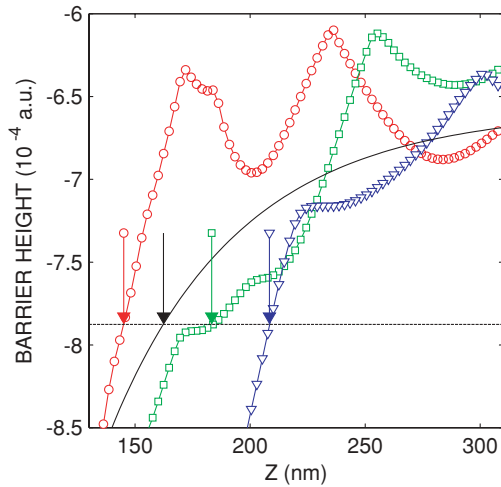
FIG. 3. (Color online) Calculated height of the surface potential barrier as a function of atom-surface separation Z with ($\bigcirc,\square,\triangle$) and without (—) stray fields present for three different incoming atom trajectories and an angle of incidence $\alpha = 13°$. An external ion collection field of 550 V cm^{-1} is applied. The horizontal dashed line indicates the energy of an $n = 26$ Rydberg atom in the applied field, the arrows the ionization distances.

the energy of the electron, which is simply taken to be the Stark energy in the applied ion collection field. The energy of a particular initial n state, which lies at the bottom of its respective Stark manifold, initially decreases with increasing applied field and, for the low-m states studied here, varies approximately as

$$E = -\frac{1}{2n^2} - \frac{3}{2}n(n-1)F, \quad F < F_c, \quad (8)$$

until levels in the n and neighboring $n-1$ manifolds begin to cross [at a field $F_c \sim 1/(3n^5)$ a.u.], which results in the appearance of a series of avoided crossings. Assuming that, as expected for low-m states, these are traversed adiabatically as the field is increased further, only small subsequent changes in electron energy occur [22]. (The measured thresholds for direct electric field ionization are consistent with adiabatic passage at avoided crossings.) The ionization distance for any incident trajectory was taken to be that distance at which the barrier height first dips below the energy of the bound electron (see Fig. 3).

Following ionization, the trajectory of the ion is computed using a Runge-Kutta algorithm taking into account its image charge attraction, the applied ion collection field, and the stray patch fields. If the ion strikes the surface it is presumed to be lost through Auger neutralization. If not, it is assumed to be collected. By considering a variety of initial Rydberg atom velocities and impact positions, it is then possible to calculate the anticipated normalized surface ionization signal for any chosen angle of incidence and applied collection field.

IV. RESULTS AND DISCUSSION

Representative experimental results are presented in Fig. 4 together with the predictions of the simulations. In each data set, measurements undertaken at nominal angles of incidence α of $5 \pm 1.2°$ and $14 \pm 1.2°$ are compared to simulations for
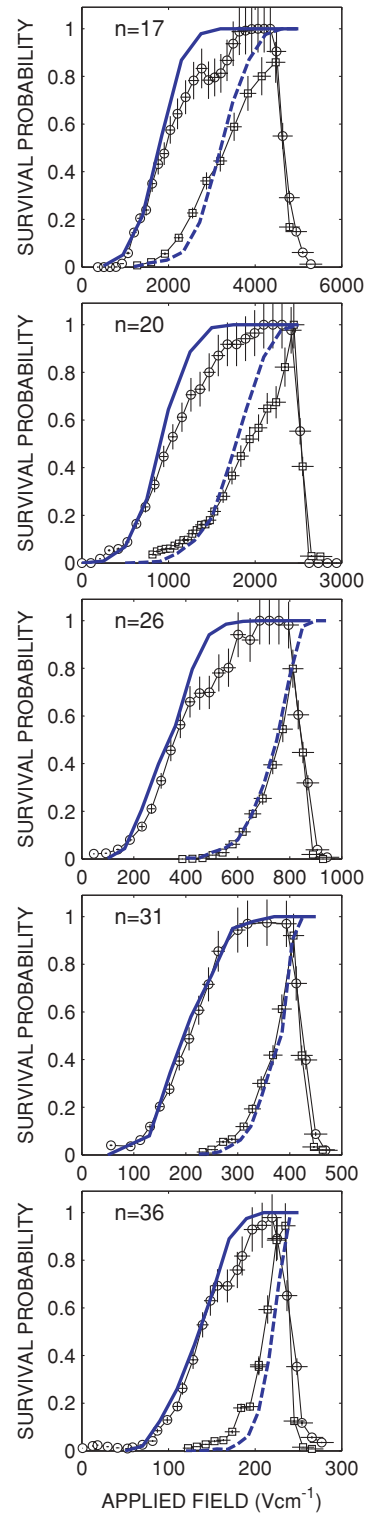
FIG. 4. (Color online) Dependence of the normalized surface ion signals on applied ion collection field for the values of n indicated. In each data set, measurements ($\bigcirc,\square$) made at nominal angles of incidence $\alpha = 5°$ and $14°$, respectively, are compared to simulations (—, - - -) for $\alpha = 4°$ and $13°$ (see text).

$\alpha = 4°$ and $13°$. The good overall agreement is remarkable considering that ionization occurs at very different atom-surface separations for $n = 17$ and 36 and that the initial ion kinetic energy perpendicular to the surface changes by

a factor of $\sim$8 as α increases from 5° to 14°. (The agreement with simulations for $\alpha = 5°$ and 14°, while good, is not quite as good as that obtained for $\alpha = 4°$ and 13°, which might be explained by the presence of a small systematic error in determining the angle of incidence.) The sharp cutoff in the surface ionization signal evident at high fields results from field ionization of the incident Rydberg atoms in vacuum before they reach the target surface. Near this cutoff, the observed normalized surface ion signals approach 1, as predicted by the simulations.

The generally good agreement between theory and experiment indicates that, when the effects of patch fields are taken into account, surface ionization is well described by a simple over-the-barrier model. The over-the-barrier model predicts that in zero applied field ionization will occur at an atom-surface separation of $\sim 3.4n^2$ a.u., consistent with the predictions of hydrogenic theory for the lowest-lying redmost states in each Stark manifold [23]. These are strongly oriented toward the surface, which results in a large electron probability density near the barrier. However, hydrogenic theory predicts that, at a given atom-surface separation, the ionization rates for blueshifted Stark states, which are oriented toward the vacuum, will be much less than for redshifted Stark states. In the case of xenon, the required ion collection fields are such that surface interactions lead to avoided crossings between states with very different spatial characteristics as the surface is approached. If these crossings are traversed adiabatically, the atom successively assumes the character of states oriented toward and away from the surface, losing much of its initial identity. On average, the electron probability density in the vicinity of the barrier is sizable, suggesting that use of a simple over-the-barrier model is reasonable.

The combined effects of stray fields and the applied ion collection field on the atom-surface separations at which ionization occurs (irrespective of whether the resulting ions are collected) are illustrated in Fig. 5 for parent $n = 26$ atoms. (Calculations for the other values of n studied here display the same general characteristics.) In the absence of stray fields, the over-the-barrier model predicts that, for a given ion collection field, all incident atoms will ionize at the same atom-surface separation (indicated by the arrows) no matter what their angle of incidence. The presence of stray fields leads to ionization occurring over a broad range of atom-surface separations. On average, stray fields increase the mean atom-surface separation at which ionization occurs. Ionization distances also increase with applied field, this being especially pronounced for fields approaching the threshold for field ionization, where atoms become more sensitive to stray fields. This is particularly evident in the results shown in Fig. 5(a) for an applied field of 750 V cm^{-1}, which amounts to $\sim$90% of that required to induce field ionization. The peak seen at large ionization distances results from ionization above regions of the surface that have large positive potential. The stray fields above such ionization "hot spots" reinforce the applied field, thereby further lowering the potential barrier and facilitating ionization. Interestingly, the relative size of this peak decreases with increasing angle of incidence. This results, at least in part, because each incident atom samples a smaller area of the target surface and is less likely to sample an ionization hot spot.
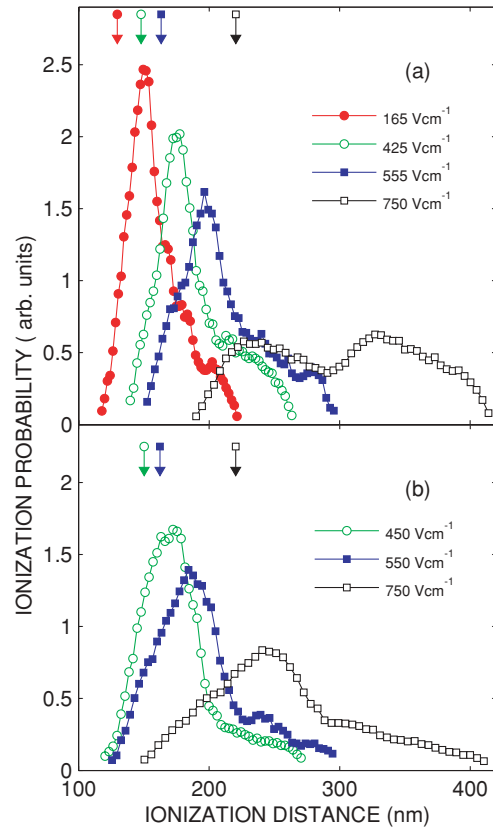
FIG. 5. (Color online) Predicted distribution of atom-surface separations at which ionization occurs for parent $n = 26$ atoms incident at (a) $\alpha = 4°$ and (b) $\alpha = 13°$ and the applied ion collection fields indicated. The arrows indicate the anticipated ionization distances in the absence of stray fields (see text).

V. SUMMARY

The present work shows that, when the effects of stray electric patch fields are taken into account, ionization of xenon Rydberg atoms at surfaces is well described by a simple over-the-barrier model. It also demonstrates the important role that patch fields can play in determining the outcome of particle-surface interactions. This can be further examined using lithographically patterned electrode arrays which provide an opportunity for their control and manipulation. For example, calculations for two interleaved parallel "comblike" electrode structures having widths (and spacings) of $\sim$0.5–1.0 μm to which alternating potentials of $\sim\pm$0.5–1.0 V are applied suggest that the localized surface fields will be sufficient to allow detection of low-n ($n < 10$) Rydberg atoms. Such electrode arrangements will facilitate detailed testing of the present model and help evaluate the utility of Rydberg atoms in characterizing surface electric fields.

ACKNOWLEDGMENTS

[1] P. Nordlander, Phys. Rev. B **53**, 4125 (1996).

[2] P. Nordlander and F. B. Dunning, Phys. Rev. B **53**, 8083 (1996).

[3] P. Nordlander and F. B. Dunning, Nucl. Instrum. Methods B **125**, 300 (1997).

[4] Z. Zhou, C. Oubré, S. B. Hill, P. Nordlander, and F. B. Dunning, Nucl. Instrum. Methods B **193**, 403 (2002).

[5] C. Oubré, P. Nordlander, and F. B. Dunning, J. Phys. Chem. B **106**, 8338 (2002).

[6] F. B. Dunning, S. Wethekam, H. R. Dunham, and J. C. Lancaster, Nucl. Instrum. Methods B **258**, 61 (2007).

[7] F. B. Dunning, H. R. Dunham, C. Oubré, and P. Nordlander, Nucl. Instrum. Methods B **203**, 69 (2003).

[8] J. Sjakste, A. G. Borisov, and J. P. Gauyacq, Phys. Rev. A **73**, 042903 (2006).

[9] E. So, M. T. Bell, and T. P. Softley, Phys. Rev. A **79**, 012901 (2009).

[10] S. Wethekam, H. R. Dunham, J. C. Lancaster, and F. B. Dunning, Phys. Rev. A **73**, 032903 (2006).

[11] D. D. Neufeld, H. R. Dunham, S. Wethekam, J. C. Lancaster, and F. B. Dunning, Phys. Rev. B **78**, 115423 (2008).

[12] M. Nonnenmacher, M. P. O'Boyle, and H. K. Wickramasinghe, Appl. Phys. Lett. **58**, 2921 (1991).

[13] N. Gaillard, M. Gros-Jean, D. Mariolle, F. Bertin, and A. Bsiesy, Appl. Phys. Lett. **89**, 154101 (2006).

[14] C. I. Sukenik, M. G. Boshier, D. Cho, V. Sandoghdar, and E. A. Hinds, Phys. Rev. Lett. **70**, 560 (1993).

[15] B. C. Stipe, H. J. Mamin, T. D. Stowe, T. W. Kenny, and D. Rugar, Phys. Rev. Lett. **87**, 096801 (2001).

[16] S. Kuehn, R. F. Loring, and J. A. Marohn, Phys. Rev. Lett. **96**, 156103 (2006).

[17] J. M. Obrecht, R. J. Wild, and E. A. Cornell, Phys. Rev. A **75**, 062903 (2007).

[18] J. Labaziewicz, Y. Ge, D. R. Leibrandt, S. X. Wang, R. Shewmon, and I. L. Chuang, Phys. Rev. Lett. **101**, 180602 (2008).

[19] See also G. R. Lloyd, S. R. Procter, and T. P. Softley, Phys. Rev. Lett. **95**, 133202 (2005); G. R. Lloyd, S. R. Procter, E. A. McCormack, and T. P. Softley, J. Chem. Phys. **126**, 184702 (2007).

[20] P. Wagner, M. Hegner, H.-J. Güntherodt, and G. Sementa, Langmuir **11**, 3867 (1995).

[21] J. D. Jackson, *Classical Electrodynamics*, 3rd ed. (Wiley, New York, 1998), Chap. 2, Sec. 9, p. 70.

[22] T. H. Jeys, G. W. Foltz, K. A. Smith, E. J. Beiting, F. G. Kellert, F. B. Dunning, and R. F. Stebbings, Phys. Rev. Lett. **44**, 390 (1980).

[23] N. N. Nedeljkovic and Lj. D. Nedeljkovic, Phys. Rev. A **72**, 032901 (2005).